Perception Testing in Fog for Autonomous Flight

George E. Gorospe Jr.*
NASA Ames Research Center, Moffett Field, CA, 94043

Elihu Deneke†, Brian J. Redman‡, Christian A. Pattyn§, Brian Z. Bentz¶, John D. van der Laan‖, and Jeremy B. Wright**
Sandia National Laboratories, Albuquerque, NM, 87123

Daniel R. Hart††
NASA Glenn Research Center, Cleveland, OH 44135

Nicholas Cramer‡‡, Corey Ippolito§§, and Kelley Hashemi¶¶
NASA Ames Research Center, Moffett Field, CA, 94043

As the path towards Urban Air Mobility (UAM) continues to take shape, there are outstanding technical challenges to achieving safe and effective air transportation operations under this new paradigm. To inform and guide technology development for UAM, NASA is investigating the current state-of-the-art in key technology areas including traffic management, detect-and-avoid, and autonomy. In support of this effort, a new perception testbed was developed at NASA Ames Research Center to collect data from an array of sensing systems representative of those that could be found on a future UAM vehicle. This testbed, featuring a Light-Detection-and-Ranging (LIDAR) instrument, a long-wave infrared sensor, and a visible spectrum camera was deployed for a multi-day test campaign in the Fog Chamber at Sandia National Laboratories (SNL), in Albuquerque, New Mexico. During the test campaign, fog conditions were created for tests with targets including a human, a resolution chart, and a small unmanned aerial vehicle (sUAV). This paper describes in detail, the developed perception testbed, the experimental setup in the fog chamber, the resulting data, and presents an initial result from analysis of the data with the evaluation of methods to increase contrast through filtering techniques.

I. Nomenclature

UAM	=	Urban Air Mobility
$LIDAR$	=	Light-Detection-and-Ranging
$SWIR$	=	Short-wave Infrared
$LWIR$	=	Long-wave Infrared
MOR	=	Meteorological Optical Range
LWC	=	Liquid Water Content
HPF	=	High Pass Filtering
BF	=	Bilateral Filtering
IFT	=	Inverse Fourier Transform

*Senior Research Engineer, Intelligent Systems Division, MS 269-3 NASA Ames Research Center, Moffett Field, CA, 94043, AIAA Member
†Senior Member of Technical Staff, Real-time Computing Research, Albuquerque, NM, 87123
‡Senior Member of Technical Staff, Counter-Autonomy Intrusion Det., Albuquerque, NM, 87123
§Intern Year Round - RD Grad, Weaponization & Signature RD, Albuquerque, NM, 87123
¶Senior Member of Technical Staff, Applied Optical/Plasma Science, Albuquerque, NM, 87123
‖Principal Member of Technical Staff, PD Remote Sensing, Albuquerque, NM, 87123
**Principal Member of Technical Staff, Weaponization & Signature RD, Albuquerque, NM, 87123
††Research Electronics Engineer, Photonics and optics Branch, NASA Glenn Research Center, Cleveland, OH 44135, AIAA Member
‡‡Aerospace Research Engineer, Intelligent Systems Division, MS 269-3 NASA Ames Research Center, Moffett Field, CA, 94043, AIAA Member
§§Aerospace Scientist, Intelligent Systems Division, MS 269-3 NASA Ames Research Center, Moffett Field, CA, 94043, AIAA Member
¶¶Autonomous Systems Technical Lead, Intelligent Systems Division, MS 269-3 NASA Ames Research Center, Moffett Field, CA, 94043, AIAA Member

DFT	=	Discrete Fourier Transform
$IDFT$	=	Inverse Discrete Fourier Transform
CEF	=	Contrast Enhanced Filtering
DVE	=	Degraded Visual Environment

II. Introduction

Urban Air Mobility (UAM) is an emerging concept for air transportation involving novel personal transportation vehicles providing on-demand flights in urban and suburban locations. The UAM concept stands to increase both the number of vehicles and the complexity of the National Airspace System (NAS). As a result, there exists several technical and policy challenges to achieving the envisioned operations for UAM in a safe and sustainable manner. NASA and Sandia National Laboratories (SNL) are actively exploring these technical challenges to both identify technology capability gaps and influence technology development that may reduce risk and promote flight safety. Towards this end, we have performed principal research in perception systems, including the development of a novel Perception Testbed at NASA Ames Research Center, in Moffett Field, CA. SNL has led efforts to develop a state-of-the-art fog chamber (SNLFC) facility capable of generating a range of fog conditions which are well characterized [1, 2] and have used the facility to further develop computational imaging capabilities in light scattering media [3–6]. Under the Transformative Tools and Technologies (T3) project, funded by the Aeronautics Research Mission Directorate (ARMD), a new perception testbed was both built and deployed for tests at the SNLFC. Data from this perception testbed will enable researchers to better understand the performance of common perception sensors in degraded visual environments (DVE) and will benefit the development of new methods for filtering or transforming the data to mitigate the effects of fog.

The Advanced Air Mobility (AAM) operations concept involves widespread, aerial transportation of people and goods within the NAS. Furthermore, the operations concept for UAM, included in AAM, will incorporate varying levels of vehicle autonomy, leading up to full autonomy without a human pilot. The human pilot traditionally observes information from the vehicle and the environment, reasons on this information, and acts to carry out the flight operations while preserving safety. Removing the pilot creates new requirements on the vehicle's perception and reasoning systems for new capabilities to ensure safe, efficient, and accessible transportation. Furthermore, expectations for nearly all-weather flight and nighttime flight add to the burden on the vehicle.

We have previously evaluated these requirements in the context of detect, track, and avoid operations [7]. This evaluation of current custom-off-the-shelf sensing systems and their distance of detection identified important trade offs between increasing the field of view of the sensors and their overall resolution. Additionally, the power levels for the sensors and update rates were also an important trade off to weigh in using these types of sensors. Considering both static and dynamic obstacle perception, the range of perception sensors must be sufficient to enable the completion of all steps of the detect and maneuver to avoid process [8].

For more than five decades engineers and researchers have studied perception systems for aircraft featuring different levels of autonomy [9]. Perception objectives generally include position/altitude estimation or object detection/identification. In the 90's [10], demonstrated the use of vision based navigation supported by GPS information for an autonomous helicopter. Singh later made significant additions to the field in the development of methods for wire detection, landing zone hazard detection, and operation in GPS denied locations [11].

This communication will first detail the development of the perception testbed then outline the experiment structure before presenting examples of the experiment results. Finally, the conclusion is presented with analytical results, and future work.

III. Development of the Perception Testbed

The technology used to sense the vicinity of the UAM vehicle and the flight path is of particular importance and also drives the development of other efforts, including sensor fusion, object detection, identification, and tracking. Sensors of this nature have seen rapid development through their use on self-driving vehicles. Common sensors used for this task include visual spectrum cameras, infrared spectrum sensors, radio detection and ranging (RADAR) units, and light detection and ranging (LIDAR) units. Each of these sensors have individual strengths and weaknesses including sampling rate, sensor size, resolution, and may be further modified with optical magnification. Furthermore, certain tasks such as object detection may rely on information from multiple sensors. Thus, it is important to characterize sensor performance for several different sensors in varied environments.

Expanding on our previous work in exploring the capabilities and gap analysis of a conceptual perception system for an autonomous urban mobility aircraft, we decided to collect three sensors representative of such a conceptual system [7]. These sensors include a visual spectrum camera, an infrared spectrum sensor, and a LIDAR unit. Together with accompanying data acquisition computers and time synchronization equipment a new perception testbed was developed.

The primary goal of the developed perception testbed is the evaluation of perception systems in the context of AAM vehicle operations, specifically operations in a DVE. To this end, the information collected by the testbed is also useful in developing new image processing methods for mitigation of environmental effects, sensor fusion algorithms, and object detection methods. Collected data from the testbed was produced by the following sensing systems:

- The FLIR Blackfly model BFS-U3-50S5C, 5-megapixel camera was used to collect visible spectrum data with the Fujinon 15 mm 1/3-inch CS mount lens. The camera has a resolution of 2448x2028 pixels, and the lens has a 32° horizontal and 24° vertical field of view. Example presented in Fig. 1.
- The FLIR Boson 640 was used with a 73 mm lens to collect LWIR infrared data between the ranges of 8 μm and 14 μm or temperatures between 140 °C (high gain) and 500 °C (low gain). The Boson has a resolution of 630 x 512 pixels, and the lens has a 6° field of view. Example presented in Fig. 2.
- The AEye 4Sight M LIDAR unit was also used on the perception testbed to collect range data up to 300 meters from the sensor. The 4Sight M has a 60° by 30° baseline field of view, with a resolution of 0.1° in both the horizontal and vertical axis. The sensor also has a range accuracy of +/- 2.5 cm at 50 meters on a target with 10% reflectivity. Although the 4Sight M has several application specific scan patterns, the full scan pattern was used throughout testing. Example presented in Fig. 3.

Data acquisition from the sensors was done via two Intel NUC small form factor computers synchronized with a GPS Time Server from Time Machines Inc. The Robot Operating System or ROS was used to coordinate the data collection. With ROS, a single command initiated the separate software commands to begin collection with the FLIR drivers. Separately, AEye's dedicated software was used to select scan patterns for the LIDAR, then initiate or terminate data collection.

IV. Experimentation

During the development of the Perception Testbed, we defined requirements for sensor evaluation testing, including tests in both optimal conditions and a DVE. After the completion of the testbed in May of 2021, the perception testbed was deployed to the SNLFC at the Sandia National Laboratories in Albuquerque, New Mexico. Within the chamber, which measures 180 feet long, by 10 feet tall, and 11 feet wide, various species of fog, including coastal fog, maybe repeatedly produced. The fog produced in the chamber creates especially challenging conditions for visual sensors like those selected for the perception testbed.

The experiment design for the deployment of the Perception testbed to the SNLFC included tests for evaluating effective resolution of the sensors, tests featuring a small UAV representative of an object detection and identification task, and tests with a moving human target. To complete these scheduled tests, we assembled or acquired three different targets. The first target, a USAF 1951 resolution test chart with variable temperature black body, was provided by the SNL staff. This resolution test chart is characteristic of the test chart originally defined by the U.S. Air Force in 1951. It features target patterns of varying sizes that consist of three parallel bars. These targets are all assembled on the chart and oriented either horizontally or vertically in a regular pattern of decreasing size. Behind the test chart is a blackbody which can be set to a desired temperature. The second target is a small, UAV chassis with six motors, perched on a standard camera tripod. During testing, the UAV's propellers were removed along with most of the control hardware. This allowed the manual control of the motors with a single servo control board outputting a pulse width modulated signal. As a result, the UAV motors could be operating during testing, and thus, become warm relative to the environment and more visible on the long-wave infrared sensor. The final target used in testing was a human who walked up and down the length of the SNLFC during the fog tests.

While ambient lighting conditions within the chamber could be controlled with a switch, the characteristics of the fog, including particle size and concentration, are less easily controlled. Whereas SNLFC can produce any of several species of fog, for all tests the fog species remained the same species, referred to as SNL Fog 1. The nature of the fog, a slowly dissipating vapor condensate, means that baseline experiments are typically carried out before fog tests. A new baseline test was conducted each time we changed the experiment configuration by introducing a new target or making a significant change to the testbed, for example, adjusting a lens. These baseline tests are relatively short, typically five minutes in duration. After baseline tests, fog tests were performed. Each fog test followed a specific sequence of events, first the fog spray was initiated to start filling the clear chamber with fog. During the spray, data collection was initiated on the perception testbed. Data collection continued until transmissometer data showed the transmission values leveling off, signifying a steady-state fog condition.. Variation in ambient temperature and other factors can result in slower dissipation of fog and longer experiments.

V. Experiment Results

During four days of testing at the SNLFC, nearly two terabytes of data were collected between the data acquisition computers. This data is composed of images and point cloud documents depicting the more than 30 baseline and fog experiments carried out in the chamber. The duration of these experiments vary based on the type of experiment. Calibration or baseline tests, as showcased in the example baseline run Fig. 4, are designed to capture the performance of the testbed sensors, typically only lasting a few minutes. Fog experiments last much longer and often capture the sequence where fog is sprayed into the chamber, the end of the spray, and the slow dissipation of the fog which can last between one to two hours. As a result, the data sets for fog experiments are much larger than baseline experiments while both contain the same data elements.

All baseline tests and fog experiments resulted in the same data elements from the Perception testbed. The visible spectrum camera produced .jpg files, the longwave infrared sensor produced .tff files, and the LIDAR produced both point cloud data in .csv format and thumbnail images in .jpg format. In addition to these data products collected by the testbed, SNL's own fog characterization equipment within the SNLFC also produced data depicting the fog particle size distribution and the meteorological optical range (MOR). These files are in the form of .csv files and are produced by a Spraytec instrument from Malvern Instruments and a transmissometer built by the engineers at SNL. The Malvern Spraytec utilizes laser beam diffraction to measure particles drawn across it's detector by an inhalation cell accessory on the instrument. Drawing the particles at a flow rate of 25 liters per minute the Spraytec can size particles from 0.1 μm to 2000 μm in diameter [12].

Fig. 1 Example data from the FLIR Blackfly visible spectrum camera. Images depict a sUAV on a tripod (left), human (center), and resolution test chart (right). Image brightness and contrast adjusted for publication.

VI. Data Analysis

The SNLFC leverages a Spraytec$^{\text{TM}}$ laser diffraction particle sizer from Malvern Instruments and an internally built transmissometer to characterize the generated fog. A schematic is provided showing the general instrument layout of test conditions in Fig. 5. This in turn allows us to correlate spatial degradation as a function of both fog characterization and time. The Spraytec$^{\text{TM}}$ particle sizer uses a fan to draw in particles to a laser beam where the diffraction pattern is measured via a proprietary detector array. A particle size distribution is recorded consisting of diameters ranging from 0.1 to 2000 μm. The deployed transmissometer measures transmission at three bands (532 nm, 1550 nm, and 9.68 μm), which respectively represent visible, mid-wave, and long-wave measurements. The measurements are taken at a fixed distance between the emitters and receivers. Transmission values are determined by the ratio of a measured radiant flux in fog to the same measurement taken without the presence of fog. The transmission data is used to calculate metrics that further characterize time varying fog along with the Spraytec$^{\text{TM}}$ recorded size distribution. These metrics are

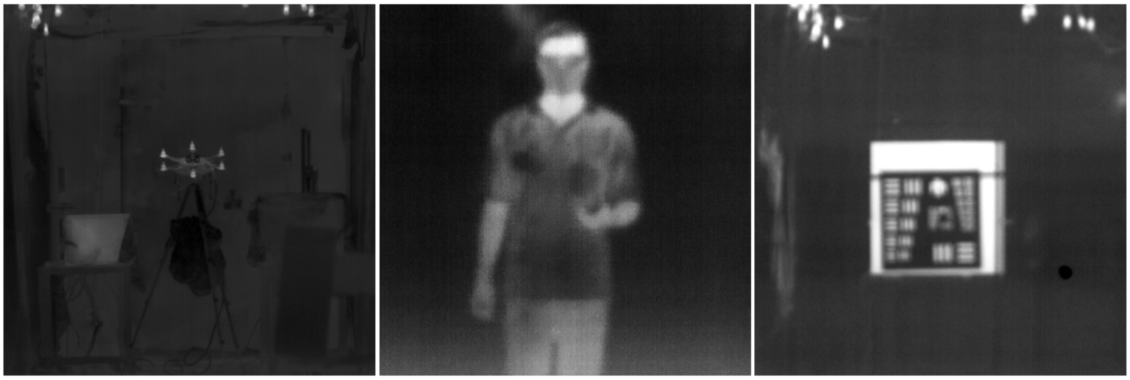

Fig. 2 Example data from the FLIR Boson LWIR sensor. Images depict a sUAV on a tripod (left), human (center), and resolution test chart (right). Image brightness and contrast adjusted for publication.

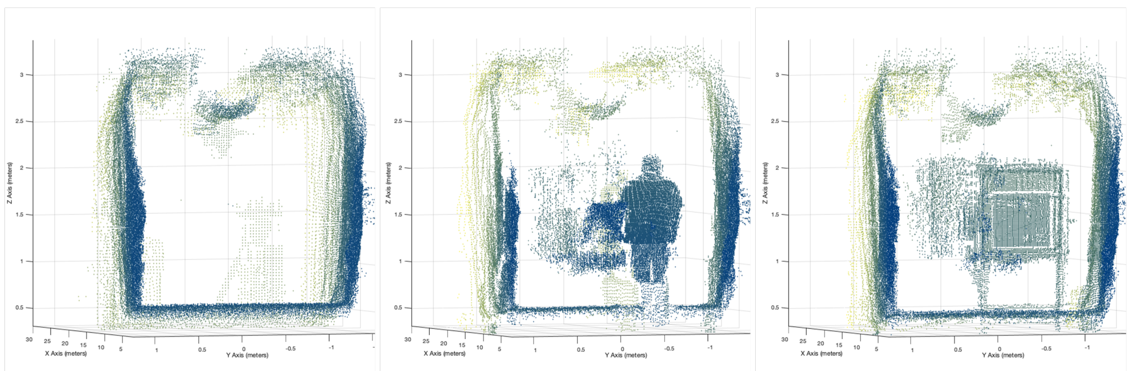

Fig. 3 Example data from the AEYE 4SightM LIDAR system. Point cloud visualizations depict a sUAV on a tripod (left), human (center), and resolution test chart (right).

presented in full by the authors of [13] and are summarized in brief here for completeness.

Meteorological optical range (MOR) is formally defined as the path length required to reduce the luminous flux in a collimated beam to 5% of its original value where the luminous flux is from an incandescent lamp at a color temperature of 2700 K [14]. In this study we measure MOR using our transmission LWIR band to measure attenuation as opposed to integrating over a 2700 K broadband spectrum. Thus, MOR is defined using Beer-Lambert law in Eq. 1.

$$MOR = \frac{-ln(0.05)}{\beta}, \tag{1}$$

Where the 5% reduction of the luminous flux relative to its original value is represented in the numerator while normalizing by the Beer-Lambert extinction coefficient, β, which is in reciprocal length units of $[\mathrm{m}^{-1}]$.

$$\beta = -ln(\frac{\phi}{\phi_o})\frac{1}{L_{trans}}, \tag{2}$$

To make the distinction of our MOR measurement at our LWIR band relative to the formal definition, we have added a subscript reflecting the band's wavelength.

$$MOR_{9.68\mu m} = L_{trans}\frac{ln(0.05)}{ln(\frac{\phi}{\phi_o})}, \tag{3}$$

Where, L_{trans} is the distance between the source and the detector, ϕ is the flux on the detector with the presence of fog while ϕ_o is the flux on the detector in the condition without fog. In addition to the MOR metric, we can calculate the liquid water content (LWC) by leveraging both the transmissometer and Spraytec$^{\mathrm{TM}}$ particle sizer. The particle sizer provides a representative size distribution of the suspended liquid particle comprising the fog media while the

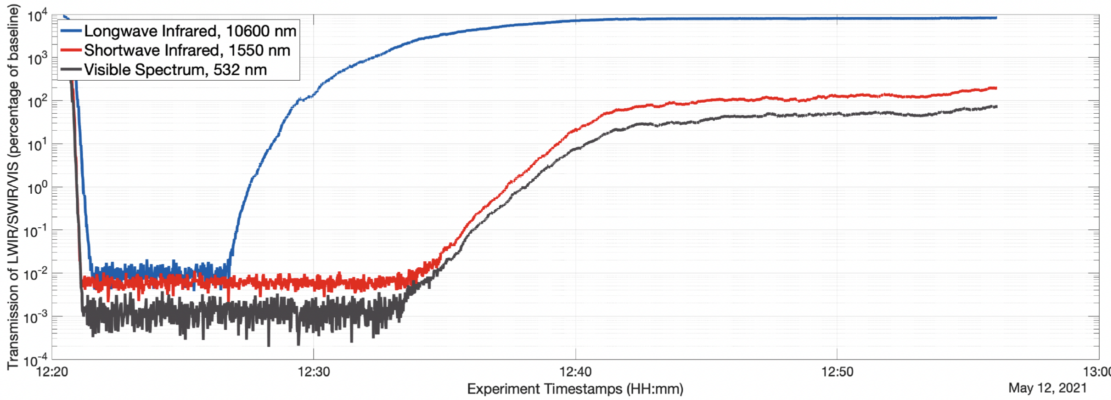

Fig. 4 Transmission of LWIR/SWIR/VIS Beams within SNLFC Starting at Baseline.

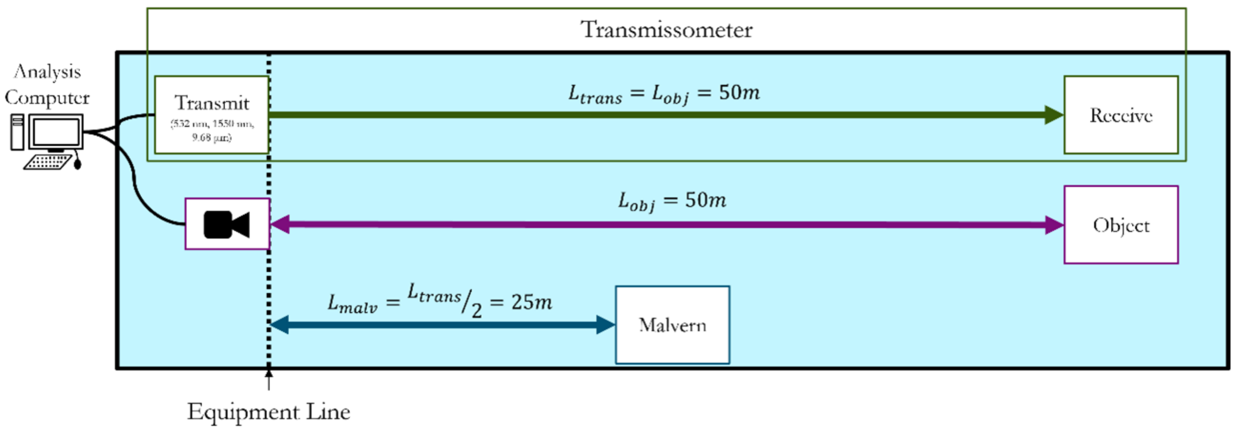

Fig. 5 Schematic of the experimental setup in the SNLFC.

transmissometer provides a quantitative measurement of the fog's density by its relative flux measurements as indicated in the numerator.

$$LWC = \frac{-2ln(\frac{\phi}{\phi_o})\frac{1}{L_{trans}}}{3\sum_i \frac{Q_i(d_i)\nu_i}{d_i}}\rho_{water}, \tag{4}$$

Where, $Q_i(d_i)$ is a unit-less extinction coefficient calculated from Mie theory [15] for a sphere of water for a given diameter from the collective particle size distribution, d_i, the percentage of the total volume contributed by diameter i is represented by, ν_i, and ρ_{water} is the density of water estimated here to be 1000 [kg/m^3].

In our study, we measured the spatial degradation due to the effects of fog by imaging an Air Force 1951 tri-bar target at varying characterized fog conditions. The tri-bar target provides 12 distinct paired bar set frequencies with both vertical and horizontal orientations. Spatial resolution is quantified by measured contrast for each frequency paired bar sets.

$$Contrast = \frac{I_{max} - I_{min}}{I_{max} + I_{min}}, \tag{5}$$

Where, I_{max} and I_{min} correspond respectively to the max and min intensity value in the local bar set spatial proximity. The idea here is that as spatial degradation increases the max and min intensity values will approach one another as illustrated in the Fig. 6.

Contrast has been measured for each respective bar set frequency while maintaining the distinction of horizontal and vertical orientation as shown in the sample plot in Fig. 7. $CTFH$ and $CTFV$ reflect respectively Contrast Transfer

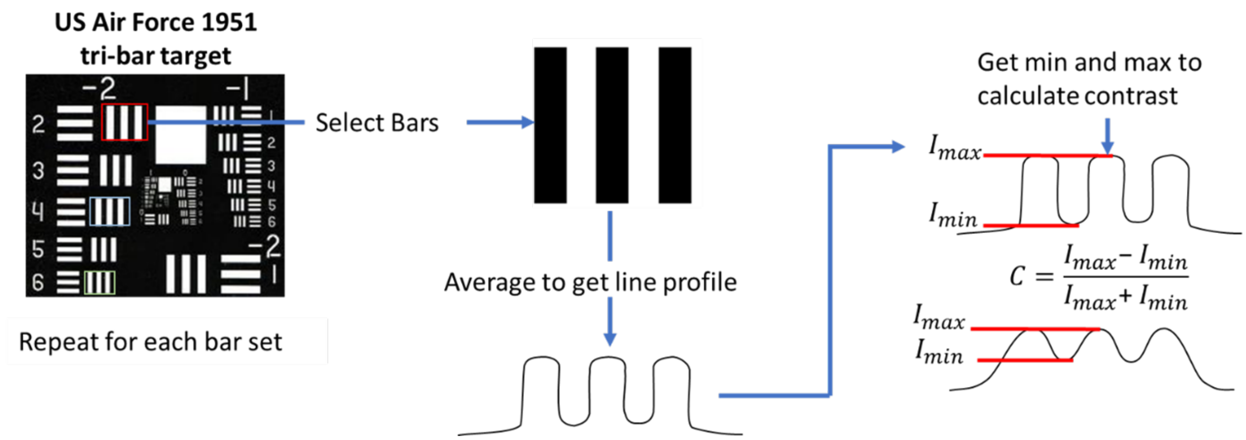

Fig. 6 Contrast is measured for all bar sets of the US Air Force 1951 tri-bar target. If contrast is high I_{max} will approach the max intensity value while I_{min} will approach the minimum intensity value, resulting in a high contrast of 1. As the image is degraded due to the presence of fog the values of I_{max} and I_{min} will approach one another resulting in a low contrast which approaches zero.

Function of horizontal and vertical sets. The point represents the discreet frequencies of the bar sets. Area under the curve (AUC) is defined as the integrated contrast across all bars set frequencies. AUC provides an overall description of spatial degradation for a high-level analysis of fogs impact on spatial information.

$$AUC = \int Contrast(f)df, \tag{6}$$

A. Image Filtering to Increase Contrast

Efforts have also been placed on recovering spatial resolution by image processing. Three image processing techniques have been implemented and compared to the original LWIR images' spatial resolution in time as characterized fog varies. These image processing techniques are high pass filtering (HPF), bilateral filtering (BF), and contrast enhanced filtering (CEF). We can transform a 2D image back and forth from spatial and frequency representation by taking the Fourier Transform (FT) and Inverse Fourier Transform (IFT), respectively [17]. It should be noted that frequency is used here in two perspectives, one concerning the spatial frequency of the bar sets and the other in reference to frequency representation after taking the FT. To aid in maintaining the distinction, frequency representation resulting from FT will be noted as FT frequency. Though, careful consideration should be taken by the reader to not confuse the two.

$$F(u,v) = \int\int_{-\infty}^{\infty} f(x,y)e^{-i2\pi(ux+vy)}dxdy, \tag{7}$$

$$f(x,y) = \int\int_{-\infty}^{\infty} F(u,v)e^{i2\pi(ux+vy)}dudv, \tag{8}$$

Where, u and v are respectively frequency representation of spatial coordinates x and y. The spatial image, $f(x,y)$, is thus transformed to its frequency representation, $F(u,v)$, by taking the FT. The IFT is used to return frequency representation back to spatial representation without loss of information. For implementation in practice, our images are discrete and thus we implement a discrete Fourier transform (DFT) and inverse discrete Fourier transform (IDFT) in place of their integral form.

$$F[p,q] = \sum_{m=0}^{M-1}\sum_{n=0}^{N-1} f[m,n]e^{-i2\pi pm/M}e^{-i2\pi qn/N};\ p = 0,1,...,M-1,\ q = 0,1,...,N-1, \tag{9}$$

$$f[m,n] = \frac{1}{MN}\sum_{p=0}^{M-1}\sum_{q=0}^{N-1} F[p,q]e^{i2\pi pm/M}e^{i2\pi qn/N};\ m = 0,1,...,M-1,\ n = 0,1,...,N-1, \tag{10}$$

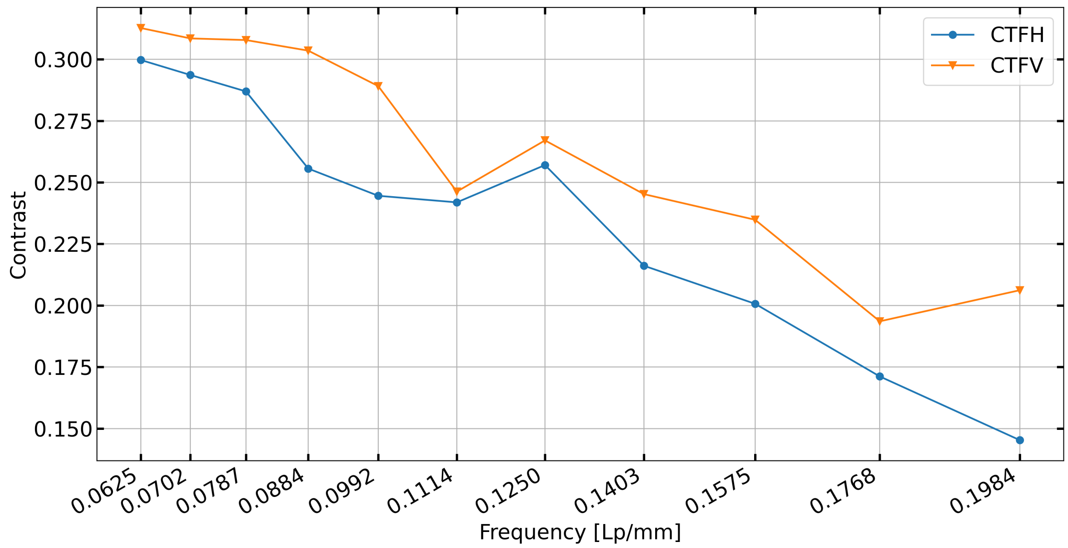

Fig. 7 Contrast is measured for each bar set, as reflected by the points, with consideration of frequency and the orientation; Vertical and horizontal sets are made distinct by color schema of yellow and blue respectively.

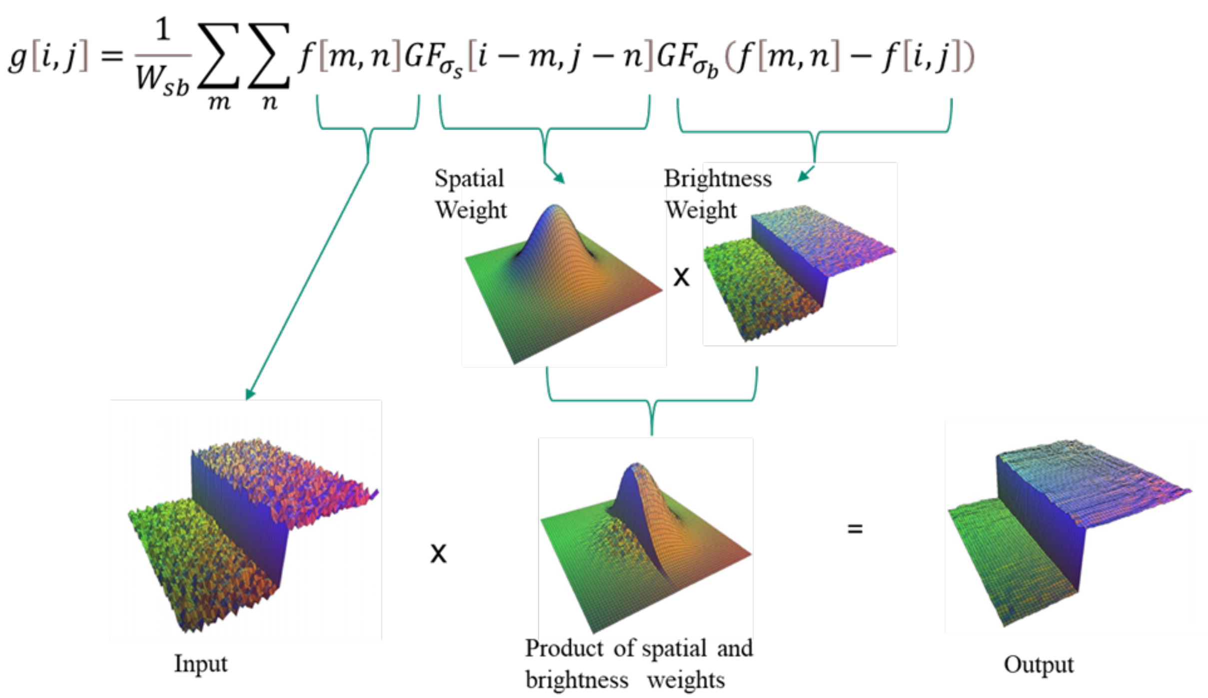

Fig. 8 The BF smooths an input image while preserving edges by applying a region dependent Gaussian kernel to both spatial and brightness regional values. The figure is reproduced from [16].

Where, p and q are respectively FT frequencies along m and n. M and N are the total number of pixels corresponding respectively to height and width. The HPF is accomplished by applying a mask that attenuates the lowest 2.6% FT frequency information as illustrated in Fig. 9. The python library NumPy was used to implement the discrete

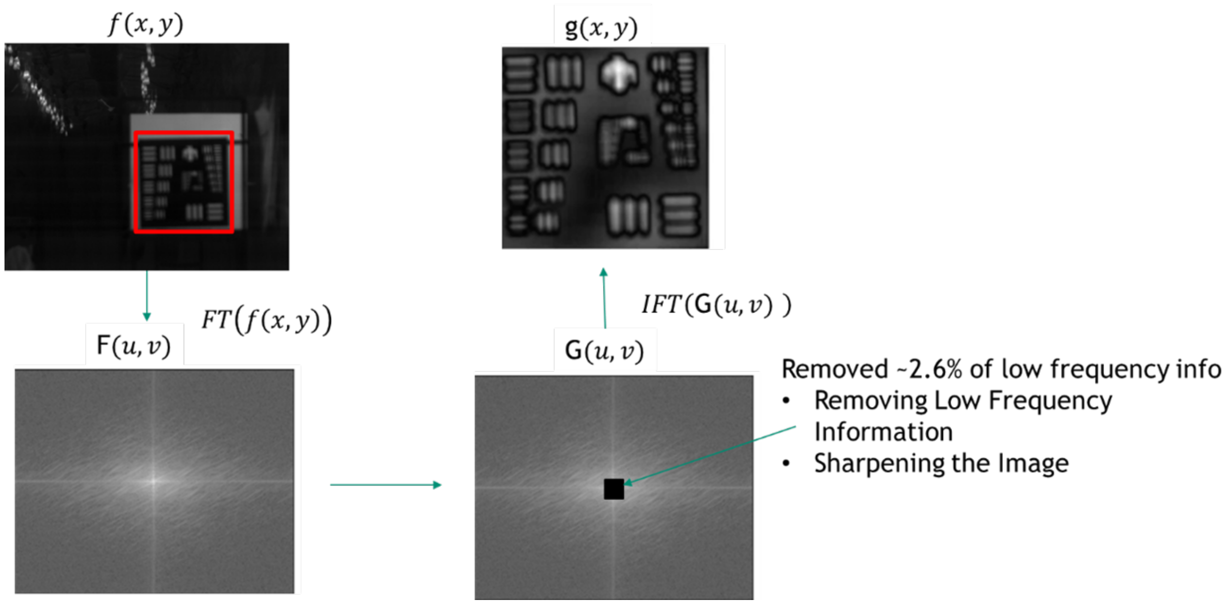

Fig. 9 HPF is applied to the target area by taking the Fourier Transform then zeroing out the lowest 2.6% frequency information. The masked spatial representation of the image is then obtained by taking the Inverse Fourier Transform which results in a sharper image.

transformations [18].

BF is a non-linear, or algorithmic in nature, image filtering technique that effectively applies Gaussian smoothing based on the similarity of neighboring pixel values. The degree of smoothing neighboring pixels is weighted by a photometric similarity Gaussian as defined below. The end effect is a filtering technique that smooths images while preserving edges [19].

$$g[i,j] = \frac{1}{W_{sb}} \sum_m \sum_n f[m,n] GF_{\sigma_s}[i-m, j-n] GF_{\sigma_b}(f[m,n] - f[i,j]), \tag{11}$$

$$GF_{\sigma_s}[i-m, j-n] = \frac{1}{2\pi\sigma_s^2} e^{-\frac{m^2+n^2}{2\sigma_s^2}}, \tag{12}$$

$$GF_{\sigma_b}[\Delta I] = \frac{1}{2\pi\sigma_b^2} e^{-\frac{\Delta I^2}{2\sigma_b^2}}, \tag{13}$$

$$W_{sb} = \sum_m \sum_n GF_{\sigma_s}[i-m, j-n] GF_{\sigma_b}(f[m,n] - f[i,j]), \tag{14}$$

Where, i and j are the indices of the pixel under consideration and m and n are the indices of the neighboring pixel we sum that fall in range of the applied kernel. GF_{σ_s} and GF_{σ_b} are Gaussian functions applied considering spatial distance and relative brightness respectively. The intuition here is that GF_{σ_b} function as the weight of what would be a common Gaussian filter based on the difference in intensity values of the pixel under consideration, $f[i,j]$, and its neighbor, $f[m,n]$. To reflect the brightness difference of neighboring pixels, let $\Delta I = f[m,n] - f[i,j]$. If the difference is large, as would be the case in the presence of an edge, GF_{σ_b} will attenuate the effects of the spatially dependent Gaussian function, GB_{σ_s}. If the intensity values are relatively close in value a higher weight is returned from GF_{σ_b} resulting in more smoothing by GF_{σ_s}. The normalizing weight, W_{sb}, is equal to the sum of the products of GB_{σ_s} and GF_{σ_b} so that the brightness is unchanged by the applied filter but only redistributed. Fig. 8 further breaks down the BF expression by term with a visual illustration.

The CEF was implemented by equalizing the intensity histogram. We accomplish intensity histogram equalization by taking the following steps [20]. First, we compute the probability of occurrences in an image, $p(n_i)$, for the pixel intensity value, n_i.

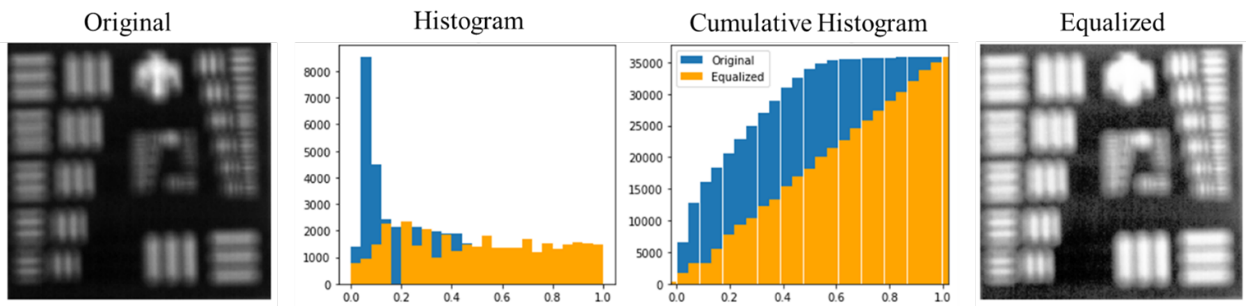

Fig. 10 Contrast enhancement filtering via histogram equalization: (right) is a long-wave image of the tri-bar set target without the presence of fog, (center left) presents a histogram of intensity values for the original and equalized images, (center right) is the cumulative histogram for both the original and equalized images, and (right) presents the resulting equalized image.

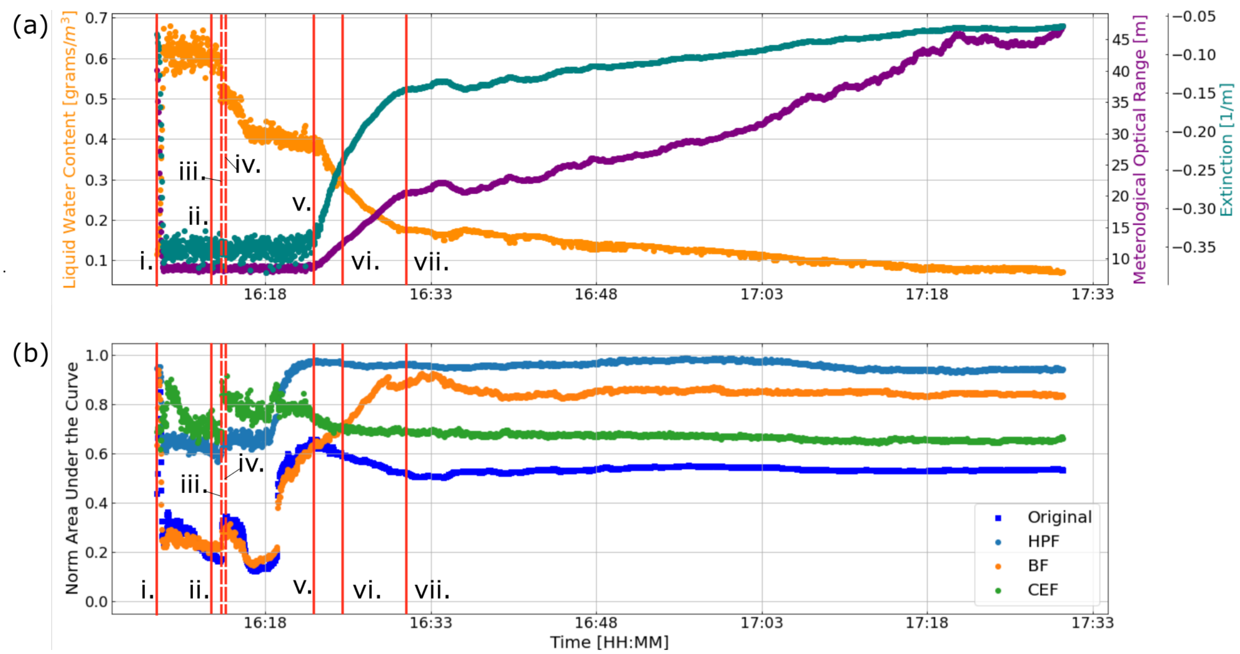

Fig. 11 The spatial resolution of the images as measured by the AUC metric is presented here as a function of fog characterization. (a) presents the fog characterization via metrics LWC, MOR, and extinction coefficient β. The AUC metric has been max normalized for each respective image set and is presented in (b). Time slice have been labeled via roman numerals that correspond to images presented in Fig 12-13.

$$p(n_i) = \frac{\text{number of pixels with intensity } \mathrm{n_i}}{\text{total number of pixels}};\ 0 \leq n_i \leq 1 - L, \tag{15}$$

Where, the intensity ranges from 0 to $L - 1$ and L is the number of possible intensity values. The histogram equalization of image f to the histogram equalized image g is as follows.

$$g_{i,j} = floor\big((L-1)\sum_{n_i=0}^{f_{i,j}} p(n_i)\big), \tag{16}$$

Where $floor$ rounds down the transformed intensity values to their nearest integer and the term $\sum_{n_i=0}^{f_{i,j}} p(n_i))$ represents the cumulative distribution function. We have max normalized the intensity values so that 1-L is equal to 1, then our intensity value distribution is shown in Fig. 10 (center left) of our target in none fog conditions for illustration purposes. It is seen that by applying the equalization to our original image, we transform our original intensity distribution values from a skewed right distribution to a uniform distribution resulting in an equalized image as reflected by both the original and equalized cumulative distribution functions in Fig. 10 (center right). The original image reaches the total count near the halfway mark of possible intensity values while the equalized image has a near linear slope along the cumulative direction reflecting the balanced intensity representation in the equalized image. The intuition here is that we will improve our contrast by gaining utility of the intensity range via balanced representation of intensity values.

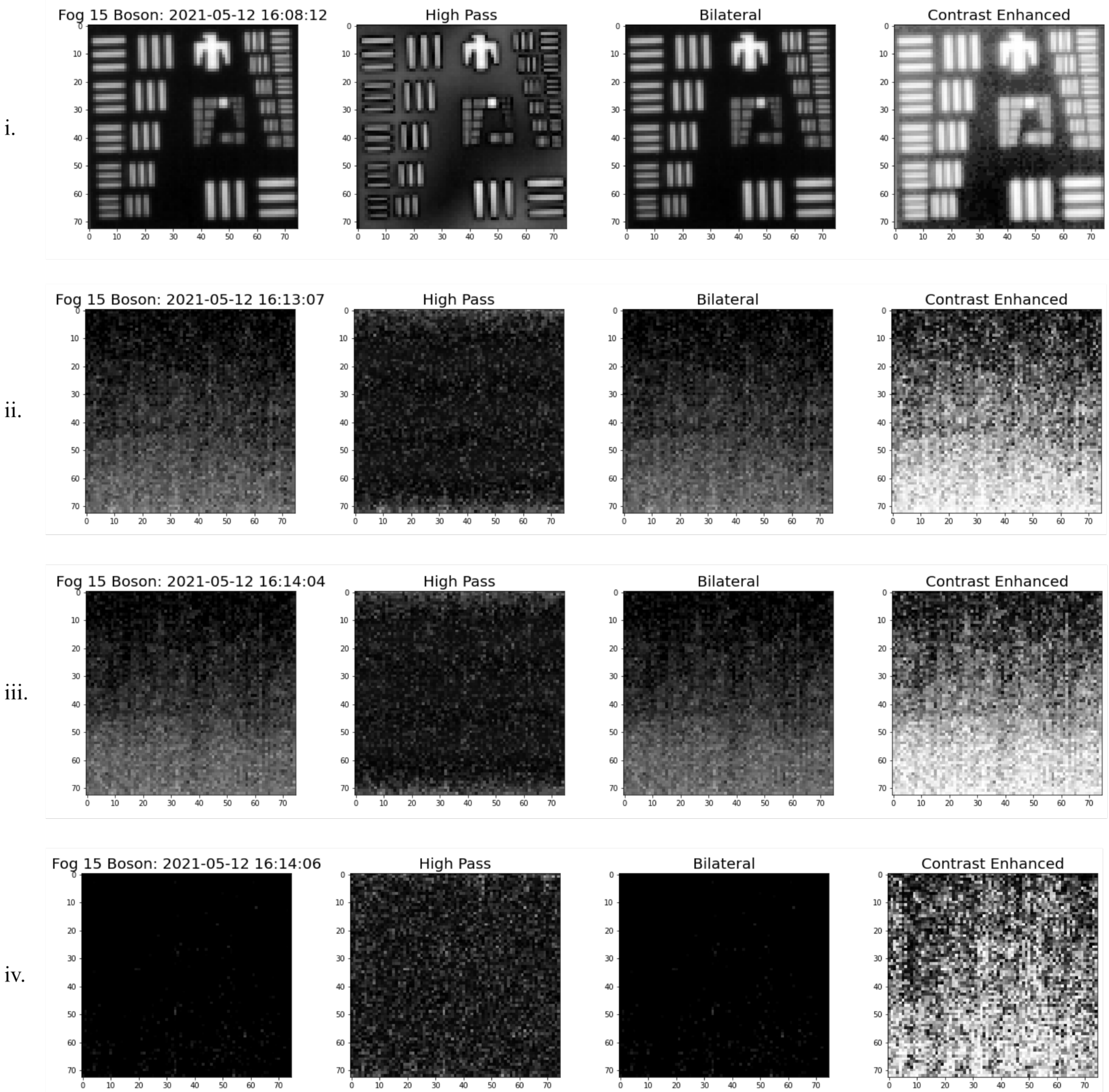

Fig. 12 Image snapshots are presented in ascending order in the temporal dimension for each image set that is considered. Each row of images corresponds to labeled slices which are also presented in Fig. 11. The image sets are represented by the columns at varying timestamps, and they consist of the original images (left), HPF (center left), BF (center right), and CEF (right). The initial 4 slice are presented, here, in Fig. 12 while the remain slices are presented in Fig. 13.

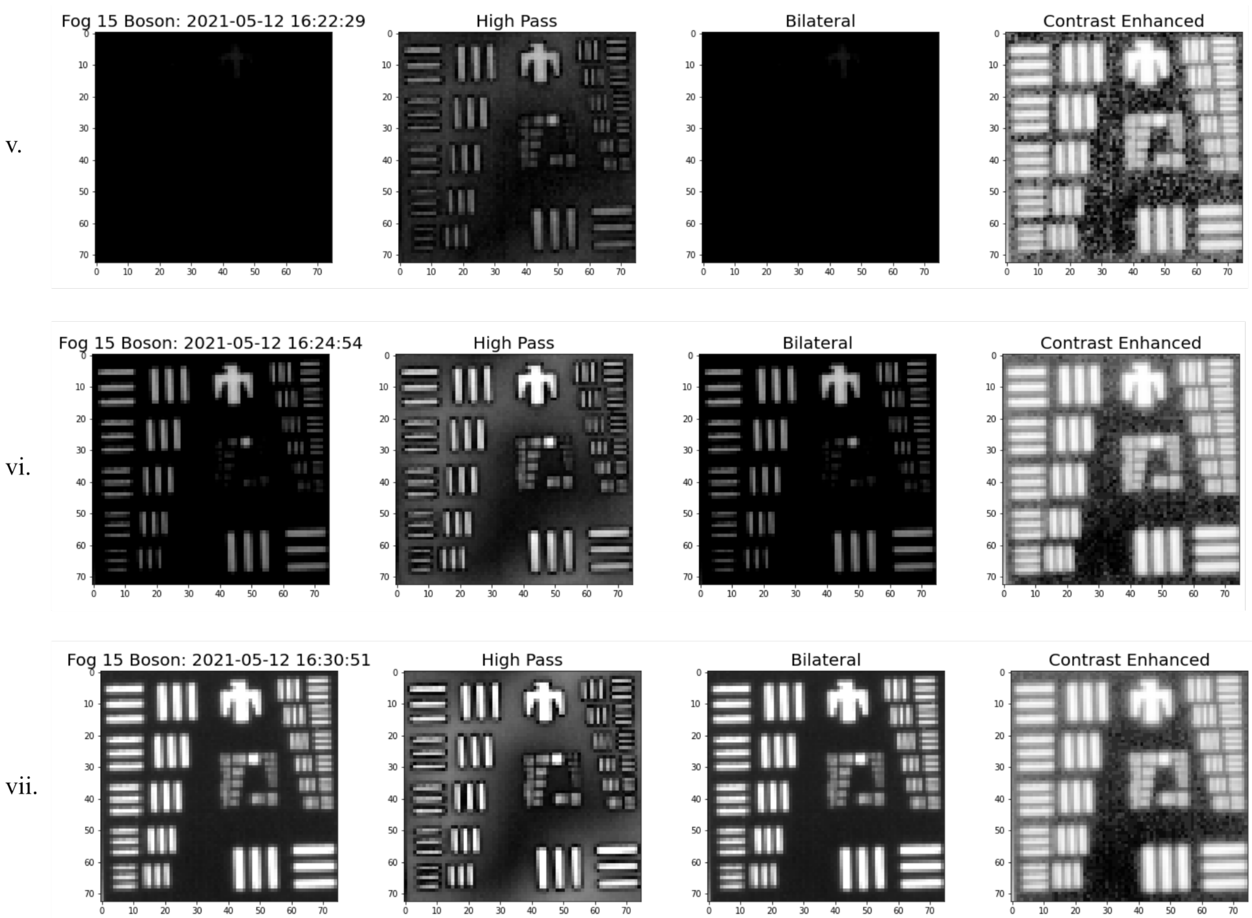

Fig. 13 The remaining image slices that follow from the image slices presented in Fig. 12.

Select time slices have been presented in Fig. 11, where in Fig. 11(a) we present the characterized fog conditions via LWC, MOR, and Extinction coefficient β, and in Fig. 11(b) we present the max normalized AUC metric where the max is taken respectively for each image set and applied accordingly for normalization. The time slices have corresponding images in Fig. 11 - 13 which include the original image and the processed images of HPF, BF, and CEF respectively. Slice (i.) presents the initial image before the start of spray. The density of the fog, as reflected by LWC, quickly reaches its max value before it begins to decay starting at slice (ii.). Slice (iii.) and (iv.) show that the LWIR camera periodically re-calibrates to a shuttered black body, which causes a shift in all intensity values as seen in Fig. 12 (iii.-iv.). This shift causes the discontinuous jump in the metric values of Fig. 11(b) (iii.-iv). At slice (v.) spatial signal begins to recover. Notably, the spatial resolution of HPF recovers relatively quicker than its counter parts as reflected in the AUC metric in Fig. 11(b) since HPF reaches max norm AUC before slice (v.) and can be visibly identified in Fig. 13. CEF also seems to recover signal nearly as well as HPF when observing Fig. 13(v.), though according to the AUC metric, spatial resolution remains at the noise floor throughout the test duration. This may be due to the regions of the tri-bar sets are over saturated resulting in a loss of contrast. The dark partitioning regions of the bar sets do not maintain their low intensity value after the histogram equalization. They instead rise as reflected by the brighter gray color causing the intensity values of the white strips and the dark partitions to approach one another. This loss in contrast is seen throughout the test independent of fog conditions. At slice (vi.), signal in the original and BF images begins to notably recover signal as the LWC continues to decay and MOR and Extinction Coefficient rise. By slice (vii) the original image has reached its stable max contrast value, while the BF processed images reached its peak contrast value resulting in a slightly improved but similar visual representation of the original images as can be seen in fig, 13. The take away from this exemplar study is that the sharpening of the images via HPF recovered signal quicker than all other images that were compared according to the AUC metric and maintained better contrast regionally to the tri-bar sets relative to the CEF as seen in Fig. 11 - 13.

VII. Conclusion

During the summer of 2021, a new perception testbed built at NASA Ames Research Center was deployed to the SNLFC located in Albuquerque, New Mexico. Within the chamber the testbed collected nearly 2 terabytes of data from a visual spectrum camera, long-wave infrared sensor, and LIDAR. This data depicts a variety of targets in a clear, evacuated chamber and in a dense fog. Experimental variables in lighting, target, target distance are varied across more than 24 different baseline collections. This data is now available to the public and may be accessed at the following URL: `https://workshops.larc.nasa.gov/RAM_Fog_Test/`.

Additionally, we have shown the results of image filtering in the frequency domain towards increasing image contrast. As DVE can significantly effect autonomous flight, such filtering techniques may be used to counteract these effects or may be used at the basis for further work. Future work with this data may include the development or maturation of sensor fusion methods, data driven methods for perception through fog, and the development of requirements for perception systems used in autonomous flight.

Acknowledgments

This work was performed under the NASA Aeronautics Mission Directorate, Transformative Tools and Technologies Project. Thanks also to Kimberlee Shish, Nicholas Cramer, and Chris Teubert.

This work was supported by the Laboratory Directed Research and Development program under the project "Computational Imaging for Intelligence in Highly Scattering Aerosols" at Sandia National Laboratories, a multimission laboratory managed and operated by National Technology and Engineering Solutions of Sandia LLC, a wholly owned subsidiary of Honeywell International Inc. for the U.S. Department of Energy's National Nuclear Security Administration under contract DE-NA0003525.

We thank Laura J. Lemieux and Steven M. Storch at Sandia National Laboratories for their assistance operating the SNLFC facility.

References

[1] Wright, J. B., van der Laan, J. D., Westlake, K., Bentz, B., Sanchez, A. L., and Redman, B. J., "Characterizing fog at the Sandia Fog Facility (Conference Presentation)," *Situation Awareness in Degraded Environments 2020*, Vol. 11424, edited by J. J. N. Sanders-Reed and J. T. J. A. III, International Society for Optics and Photonics, SPIE, 2020, p. 1142402. https://doi.org/10.1117/12.2561099, URL https://doi.org/10.1117/12.2561099.

[2] Bentz, B. Z., Pattyn, C. A., Redman, B. J., Zenker, J. P., Deneke, E., Sanchez, A. L., Westlake, K., van der Laan, J. D., and Wright, J. B., "Optical characterization of the Sandia fog facility for computational sensing," *Optical Sensors and Sensing Congress 2022 (AIS, LACSEA, Sensors, ES)*, Optica Publishing Group, 2022, p. LF1C.3. https://doi.org/10.1364/LACSEA.2022.LF1C.3, URL https://opg.optica.org/abstract.cfm?URI=LACSEA-2022-LF1C.3.

[3] van der Laan, J. D., Wright, J. B., Scrymgeour, D. A., Kemme, S. A., and Dereniak, E. L., "Evolution of circular and linear polarization in scattering environments," *Opt. Express*, Vol. 23, No. 25, 2015, pp. 31874–31888. https://doi.org/10.1364/OE.23.031874, URL https://opg.optica.org/oe/abstract.cfm?URI=oe-23-25-31874.

[4] van der Laan, J. D., Wright, J. B., Kemme, S. A., and Scrymgeour, D. A., "Superior signal persistence of circularly polarized light in polydisperse, real-world fog environments," *Appl. Opt.*, Vol. 57, No. 19, 2018, pp. 5464–5473. https://doi.org/10.1364/AO.57.005464, URL https://opg.optica.org/ao/abstract.cfm?URI=ao-57-19-5464.

[5] Bentz, B. Z., Redman, B. J., van der Laan, J. D., Westlake, K., Glen, A., Sanchez, A. L., and Wright, J. B., "Light transport with weak angular dependence in fog," *Opt. Express*, Vol. 29, No. 9, 2021, pp. 13231–13245. https://doi.org/10.1364/OE.422172, URL https://opg.optica.org/oe/abstract.cfm?URI=oe-29-9-13231.

[6] Bentz, B. Z., Pattyn, C. A., van der Laan, J. D., Redman, B. J., Glen, A., Sanchez, A. L., Westlake, K., and Wright, J. B., "Incorporating the effects of objects in an approximate model of light transport in scattering media," *Opt. Lett.*, Vol. 47, No. 8, 2022, pp. 2000–2003. https://doi.org/10.1364/OL.451725, URL https://opg.optica.org/ol/abstract.cfm?URI=ol-47-8-2000.

[7] Shish, K. H., Cramer, N. B., Gorospe, G., Lombaerts, T., Stepanyan, V., and Kannan, K., "Survey of Capabilities and Gaps in External Perception Sensors for Autonomous Urban Air Mobility Applications," *AIAA Scitech 2021 Forum*, 2021, p. 1114.

[8] SC-228, R. F., *Minimum Operational Performance Standards (MOPS) for Detect and Avoid (DAA) Systems*, RTCA, Incorporated, 2017.

[9] Nonami, K., "Prospect and recent research & development for civil use autonomous unmanned aircraft as UAV and MAV," *Journal of system Design and Dynamics*, Vol. 1, No. 2, 2007, pp. 120–128.

[10] Fürst, S., and Dickmanns, E.-D., "A vision based navigation system for autonomous aircraft," *Robotics and Autonomous Systems*, Vol. 28, No. 2-3, 1999, pp. 173–184.

[11] Singh, S., Cover, H., Stambler, A., Grocholsky, B., Mishler, J., Hamner, B., Strabala, K., Sherwin, G., Kaess, M., Hemann, G., et al., "Perception for safe autonomous helicopter flight and landing," *American Helicopter Society 72nd Annual Forum, West Palm Beach, Florida, USA*, 2016.

[12] Wright, J. B., van der Laan, J. D., Sanchez, A., Kemme, S. A., and Scrymgeour, D. A., "Optical characterization of the Sandia fog facility," *Degraded Environments: Sensing, Processing, and Display 2017*, Vol. 10197, SPIE, 2017, pp. 29–34.

[13] Redman, B. J., van der Laan, J. D., Westlake, K. R., Segal, J. W., LaCasse, C. F., Sanchez, A. L., and Wright, J. B., "Measuring resolution degradation of long-wavelength infrared imagery in fog," *Optical Engineering*, Vol. 58, No. 5, 2019, p. 051806. https://doi.org/10.1117/1.OE.58.5.051806, URL https://doi.org/10.1117/1.OE.58.5.051806.

[14] *Guide to Meteorological Instruments and Methods of Observation*, 1983.

[15] Bohren, C., and Huffman, D. R., *Absorption and Scattering of Light by Small Particles*, Wiley Science Paperback Series, 1998.

[16] Durand, F., and Dorsey, J., "Fast Bilateral Filtering for the Display of High-Dynamic-Range Images," *Proceedings of the 29th Annual Conference on Computer Graphics and Interactive Techniques*, Association for Computing Machinery, New York, NY, USA, 2002, p. 257–266. https://doi.org/10.1145/566570.566574, URL https://doi.org/10.1145/566570.566574.

[17] Cooley, J. W., and Tukey, J. W., "An Algorithm for the Machine Calculation of Complex Fourier Series," *Mathematics of Computation*, Vol. 19, No. 90, 1965, pp. 297–301. URL http://www.jstor.org/stable/2003354.

[18] Harris, C. R., Millman, K. J., van der Walt, S. J., Gommers, R., Virtanen, P., Cournapeau, D., Wieser, E., Taylor, J., Berg, S., Smith, N. J., Kern, R., Picus, M., Hoyer, S., van Kerkwijk, M. H., Brett, M., Haldane, A., del Río, J. F., Wiebe, M., Peterson, P., Gérard-Marchant, P., Sheppard, K., Reddy, T., Weckesser, W., Abbasi, H., Gohlke, C., and Oliphant, T. E., "Array programming with NumPy," *Nature*, Vol. 585, No. 7825, 2020, pp. 357–362. https://doi.org/10.1038/s41586-020-2649-2, URL https://doi.org/10.1038/s41586-020-2649-2.

[19] Tomasi, C., and Manduchi, R., "Bilateral filtering for gray and color images," *Sixth International Conference on Computer Vision (IEEE Cat. No.98CH36271)*, 1998, pp. 839–846. https://doi.org/10.1109/ICCV.1998.710815.

[20] Gonzalez, R. C., and Woods, R. E., *Digital image processing*, Prentice Hall, Upper Saddle River, N.J., 2008. URL http://www.amazon.com/Digital-Image-Processing-3rd-Edition/dp/013168728X.